Transparent Conductive Oxide Type Material for the Anode of Solid Oxide Fuel Cells at a Reduced Temperature

Xuelin Zhang [a], Yuan Zhang [a], Jiupai Ni [a, b], John T.S. Irvine [a, c], Chengsheng Ni [a, b] *

a College of Resource and Environment, Southwest University, Beibei, Chongqing, China, 400715

b National Base of International S&T Collaboration on Water Environmental Monitoring and Simulation in Three Gorges Reservoir Region, Chongqing 400716, China

c School of Chemistry, University of St Andrews, North Haugh, KY16 9ST, Scotland, UK

Email: nichengsheg@swu.edu.cn

Abstract: Solid oxide fuel cells (SOFCs) can be used for the high-efficiency conversion of chemical energy into electricity. The exploration of oxide anode will enhance the coking resistance and the oxidation-reduction (redox) stability comparing to the conventional Ni(O) cermet anode. An *n*-type semiconductor with electron charge carriers will be conducive to the electric conductivity, σ, in fuel conditions, but the research on *n*-type oxide electrodes is limited mostly to perovskite-type titanate that requires very high temperature and low oxygen partial pressure to provide a decent σ. Transparent conductive oxides (TCOs) with a superior σ even at room temperature are widely explored for electronic devices, but they have never been studied as the alternative oxide anode of an SOFC at a reduced temperature. An *n*-type TCO type material $ZnGa_2O_4$ (ZGO) that could be reduced at a temperature below 700 °C was used as the anode for the oxidation of H_2 and hydrocarbon (ethanol and propane) at ≤ 650 °C. ZGO provided a high σ of 1.5 and 0.33 S cm^{-1} at 700 °C and 600 °C, respectively, and the cell with ZGO anode on $Sc_{0.18}Ce_{0.01}Zr_{0.81}O_{2-\delta}$ electrolyte showed a high redox stability. The performance of the cell with ZGO/GDC (Gd_2O_3 doped ceria) anode could be enhanced by the

infiltration of 1% Ni, imparting a peak power of 574 mW cm^{-2} at 650 °C and a stable cell performance of 300 mW cm^{-2} at 600 °C for 300 hours. The cell was also found to be relatively stable under carbonaceous fuel, suppressing the carbon deposition at 600 °C. This work provided a new avenue of designing an *n*-type oxide anode that could be reduced *in situ* in the fuel condition of a low-temperature SOFC.

Keywords: solid oxide electrochemical cells; transparent conductive oxide; *n*-type semiconductor; $ZnGa_2O_4$

1. Introduction

Solid oxide fuel cells (SOFCs) are energy conversion devices that convert chemical energy into electrical energy at a temperature above 500 °C [1] and can use hydrocarbons directly as fuel with higher efficiency than traditional fossil fuel power plants,[2] but the coking on the state-of-the-art Ni-based fuel electrode will cause the deactivation of the SOFCs.[3-5] The redox of fuel cells using Ni(O) cermet electrode tends to cause the disintegration of the electrolyte, loss of electric conductivity (σ) [6,7] and the deterioration of microstructure because of the large volumetric expansion from metal Ni to NiO.[8]

An *n*-type semiconductor is a material in which electrons are the majority carriers, arising *via* a temperature-activated small-polaron hopping.[9] Although *n*-type $SrTiO_3$-based perovskites have been studied as an alternative SOFC anode, their reduction for acceptable σ can only be achieved at high temperatures (> 800 °C),[10,11] and the σ will decrease with the oxygen partial pressure, $P(O_2)$. Moreover, the electrocatalytic performance of a titanate perovskite for fuel oxidation is poor as the oxygen non-stoichiometry is generally low that limits the oxide-ion conductivity for expanded reaction sites.[12]

Transparent conductive oxides (TCOs) are a kind of materials with high light transmittance in the

visible light spectrum (380 nm< λ < 780 nm) and high σ.[13] TCO generates carriers through the doping using donors or acceptors whose energy levels are close to the conduction band or valence band. At present, TCO encompasses mainly ITO (Sn-doped In_2O_3), FTO (F-doped In_2O_3), AZO (Al-doped ZnO), etc.[14-16] $ZnGa_2O_4$ (ZGO) has a wider band gap than ITO, but the σ exceeds 10 S cm^{-1} after the reduction under H_2 at 700 °C,[17] indicating it could be reduced *in situ* under the fuel condition of an SOFC to trigger high σ as an *n*-type oxide using oxide-ion vacancy (V_O) as donor.

The low reduction temperature of ZGO fits in the need for the low-temperature SOFC (LT-SOFC) that will reduce the deterioration of the structure and electrode material.[18,19] Therefore, an *n*-type TCO type material, ZGO, was employed as an alternative oxide anode of a SOFC below 700 °C for the first time in this study. Its electrochemical performance of ZGO anode alone was found to be low because of the insufficient oxide ionic conductivity of this spinel type oxide with superficial reduction, but a high performance could be achieved by compositing with GDC and 1% Ni infiltration since ZGO provided sufficient σ for the electrons to flow.[20,21] The $Sc_{0.18}Ce_{0.01}Zr_{0.81}O_{2-\delta}$ (SSZ) electrolyte supported cell showed a high redox stability between H_2 and air. In the meantime, a stable and high performance was demonstrated in H_2 (a peak power of 300 mW cm^{-2} at 600 °C), propane and ethanol fuel using ZGO-based electrode. This work initiated a new way of designing alternative oxide anode of LT-SOFC by liaising the research on TCO type material and oxide anode, which would be important for the developing of *n*-type oxide anode with a high electronic conduction.

2. Experimental

2.1 Powder preparation

ZGO powders were synthesized by solid-state reaction method. Stoichiometric ZnO (99.99%

Macklin, China) and Ga_2O_3 (99.99% Macklin, China) were mixed using an agate and mortar and then the admixture was pressed into small discs at an isostatic pressure of 10 MPa. The discs were calcined at 1300 °C for 5 h in air and re-ground thoroughly to obtain a powdered ZGO spinel that would be refined in ethanol for 1 h using a planetary ball mill at 600 revolutions per minute.

2.2 Characterization

X-ray diffraction (XRD) was performed using a diffractometer ($K_{\alpha 1}$=1.5406 Å, Persee XD-3, China) in the 2θ range from 10° to 80° at a step size of 0.02°. The ZGO powders were reduced at different temperatures in 5% H_2 for 5 h to study the phase stability. A four-probe method using a high-precision multimeter (Keithley 2100, USA) was employed to measure the direct current σ of ZGO bars (2.10 mm x 4.11 mm x 1.31 mm) along with a zirconia-based P(O_2) sensor in the vicinity of the samples. The electric conductivity relaxation (ECR) method was used to characterize the oxygen transport rates of ZGO on the surface. The chemical surface exchange coefficient (k_{chem}) and the chemical bulk diffusion coefficient (D_{chem}) were obtained according to Fick's second law.[22,23] Thermal expansion coefficients (TECs) were characterized in air and 5% H_2 atmosphere from 30 to 700 °C using a dilatometer (PCY-1400II, Xiangtan, China). All TECs were corrected against a dense Al_2O_3 standard bar. The TEC of the pre-reduced sample in 5% H_2 at 750 °C for 5 h was measured in 5% H_2 during the heating. The thermo-catalysis of ZGO for ethanol cracking was measured using a residual gas analyzer (RGA, QIC-20, Hiden, UK): Ar (30 mL/min) bubbled through an absolute ethanol scrubber and brought the ethanol vapor into a U-shaped quartz tube containing a ZGO bed (0.2 g) and then the effluent was monitored during the heating.

Diffuse ultraviolet-visible (UV-Vis) reflectance spectroscopy of the ZGO powders was performed

on an Ultraviolet-1800 spectrophotometer (Macy, China) with a 100-mm integration sphere. X-ray photoelectron spectroscopy (XPS) was obtained on a Thermo Scientific K-Alpha+ spectrophotometer with monochromatized Al Kα X-ray ($h\nu$ = 1486.6 eV) radiation in ultrahigh vacuum (< 5 x 10^{-7} mBar). The binding energies were calibrated by using C1s peak (284.8 eV) of the adventitious carbon. Scanning electron microscopy (SEM, ZEISS Gemini 300) was used to observe the cross-sectional morphology of the ZGO/GDC-1% Ni cell anode after using ethanol as fuel. The microstructure of the surface of reduced sample was analyzed for lattice constant and elemental content using a transmission electron microscopy (TEM, JEM-F200(URP), Japan).

2.3 Fabrication and testing of SOFCs

The specific preparation process was shown in Scheme 1. SSZ electrolyte was prepared from a green tape that was sintered at 1430 °C for 5 h. The refined ZGO powders were mixed with an equal weight of vehicle containing polyvinyl butyral in terpineol to obtain a slurry. For the cathode, $Ce_{0.9}Gd_{0.1}O_{1.95}$ (GDC) nanoparticles was mixed with 20 wt % graphite as pore forming agent, and then an equal weight of the vehicle to the solids was added and mixed with the admixture to obtain slurry.

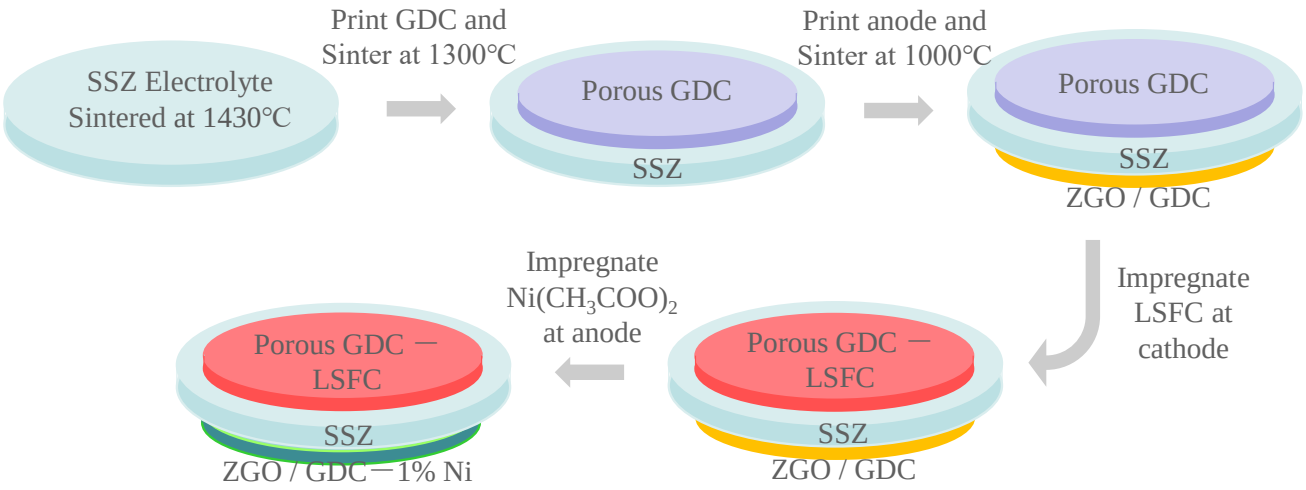

Scheme 1. Schematics for the processing of an SOFC with a ZGO/GDC-1% Ni composite anode.

The GDC slurry was first painted onto one side of the electrode and sintered at 1300°C for 2 h to prepare a porous skeleton. Afterwards, the ZGO or ZGO/GDC slurry was painted and calcined in air at 1000 °C. The GDC skeleton would be infiltrated using a 1.5 mol/L solution containing nitrate salt solution for the $La_{0.8}Sr_{0.2}Fe_{0.8}Co_{0.2}O_3$ (LSFC) cathode.[24] For some cells, 1% Ni acetate was impregnated into the anode after the preparation of cathode.

The slurry (about 46 wt %) which was prepared by mixing Ag slurry (Batch No.: 3706, SINWE, China) and 20 wt % starch was applied on both sides of the cell in a grid shape for current collection, and the Ag wire was attached to the silver paste as lead wire. The prepared cell was mounted on top of the Al_2O_3 tube using a ceramic bond and was heated to 650 °C, and then fuel was fed into the anode chamber after flushing the air with Ar flow. The H_2, propane, and methane were all fed to the anode through gas pipeline directly, while ethanol was carried into the anode chamber by using Ar to flow into the absolute ethanol scrubber so that the ethanol vapor adhered to the Ar. A Zennium *Pro* electrochemical workstation (Zahner, Germany) was used to perform electrochemical measurements, including current-voltage-power (I−V−P), and electrochemical impedance spectroscopy (EIS). The sine wave for EIS measurement was in an amplitude of 10 mV from 1 MHz to 50 mHz. The analysis of distribution of relaxation times (DRT) for the impedance spectra was presented with a regularization parameter of 10^{-3} using DRT tool.[25-27]

3. Results

3.1 Material characterizations

ZGO was a double oxide with the cubic spinel structure, which was consistent with the room temperature XRD (Figure 1a).[17] ZGO maintained the spinel structure after the reduction in 5% H_2 at

700 °C for 5 h, but the peak for β-Ga_2O_3 was shown if it was reduced obviously at 800 °C,[28] as a result of the change in the ratio of Zn/Ga due to the much higher vapor pressure of Zn causing the loss of zinc.[29,30] While the reduction process generally caused the shift of main peak towards the lower angle direction as a result of the generation of Zn^+ that was larger than Zn^{2+}.[31] A minor peak at 38.3° was observed as a result of the peak high-angle shifting of the one at 37.3° was detected for the reduced surface layer, (Zn, Ga)O_2,[32] causing a phase change if the Zn^{2+} in tetrahedron were moved to the octahedron site in a reduced state.

The σ of the ZGO spinel (Figure 1b) reached 1.5 S cm^{-1} at 700 °C, and a decent σ of 0.3 and 0.7 S cm^{-1} could be obtained even the sample was slightly reduced at 600 and 650 °C, respectively. On the other hand, the reduction of the sample at 800 °C increased the σ very little comparing to the one at 700 °C because of the decomposition of ZGO, causing the emergence of insulating β-Ga_2O_3 which could be seen that ZGO was more suitable at a low temperature SOFC. Compared with previous works (Figure 1c), such as $La_{0.2}Sr_{0.25}Ca_{0.45}TiO_3$ (LSCT)[33] and $La_{0.75}Sr_{0.25}Cr_{0.5}Mn_{0.5}O_{3-\delta}$ (LSCM)[34], the ZGO reduced at low temperature imparted a higher conductivity. For example, at 650 °C, the σ of the reduced LSCM and LSCT was about 0.43 S cm^{-1} and 0.18 S cm^{-1} respectively, while the σ of ZGO could reach 1.0 S cm^{-1}. Arrhenius plots of the σ in 5% H_2 indicated an activation energy (E_a) of 0.55 eV and 0.69 eV for the sample reduced at 700 °C and 800 °C, respectively. The error bars of the data fitting (Figure S1) were extraordinarily small to show the thermal activation of the conductivity. The higher E_a for the sample reduced at 800 °C than the one at 700 °C could be resulted from the decreased doping level as a result of Zn evaporation, causing the limitation in the charge-carrier generation. The P(O_2) dependence of conductivity at 600 °C (Figure 1d) was consistent with a typical *n*-type semiconductor. The slope for the plot of Lg(σ/ S cm^{-1}) and P(O_2) at low oxygen partial pressure was

close to −1/6 following the defect equilibrium of $[V_O^{\bullet\bullet}] \approx 1/2n$ owing to the intrinsic electronic compensation.[35]

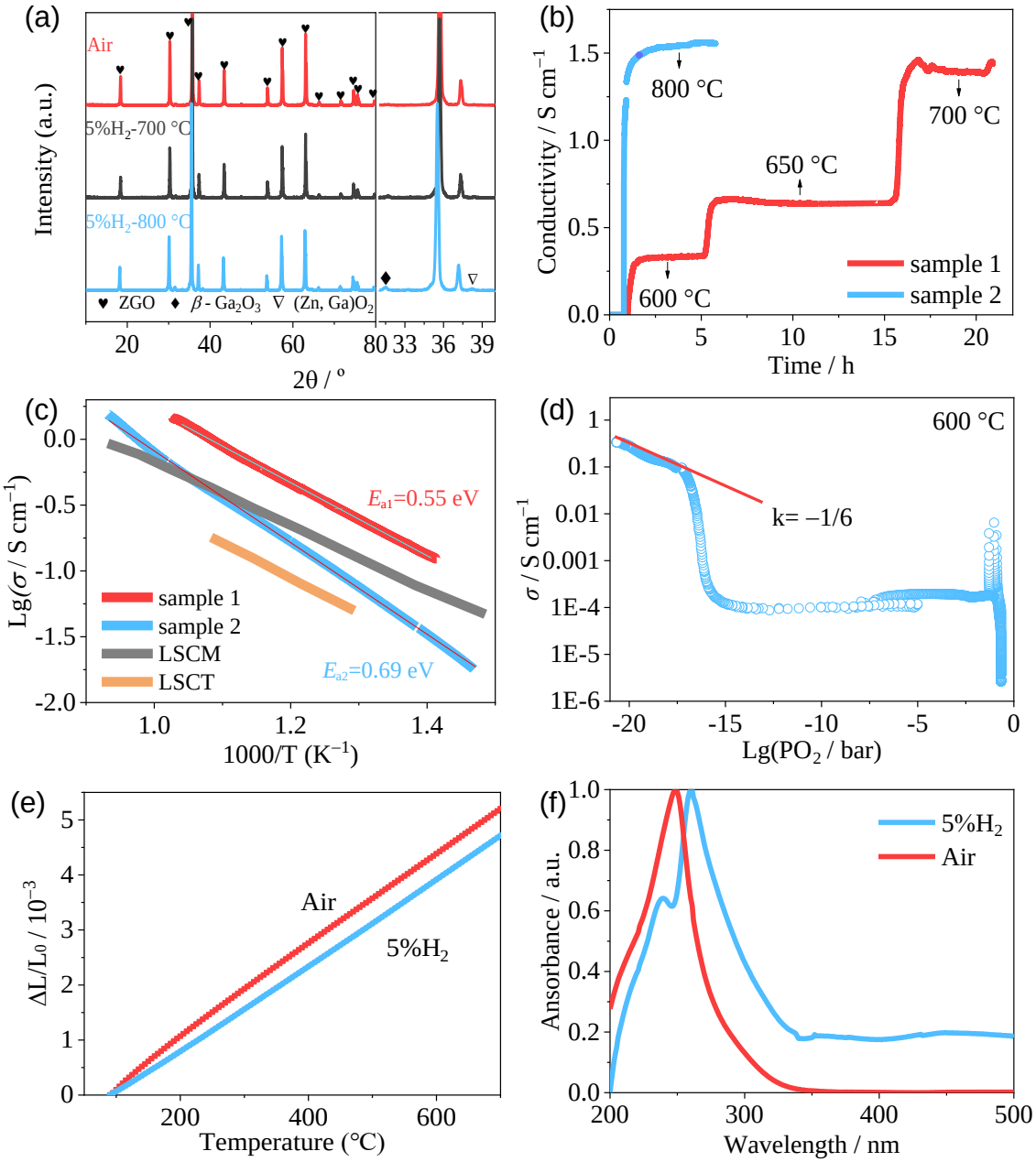

Figure 1. (a) XRDs of ZGO in Air and 5% H_2 at different temperatures and (b) σ of ZGO in 5% H_2 at different temperature. (c) Arrhenius plots of σ of ZGO after 5 h reduction under 5% H_2 flow during the cooling time in comparison with those of $La_{0.2}Sr_{0.25}Ca_{0.45}TiO_3$ (LSCT)[33] and $La_{0.75}Sr_{0.25}Cr_{0.5}Mn_{0.5}O_{3-\delta}$ (LSCM)[34]. (d) Isothermal $P(O_2)$ dependence of σ for ZGO at 600 °C during

the gas switching. (e) TEC of ZGO from room temperature to 700 °C in Air and 5% H_2. (f) UV-Vis spectra of ZGO synthesized in air and reduced in 5% H_2 at 700 °C. "Sample 1" and "sample 2" in (b, c) indicated ZGO with a final reduction temperature at 700 and 800 °C, respectively.

The dilatometry (Figure 1e) of ZGO showed a linear expansion with temperature and the TEC was slightly higher in air (8.16 ppm/K) than that of 5% H_2 (7.83 ppm/K), which was close to that of YSZ electrolyte (10.3 ppm/K). UV-Vis absorption spectroscopy (Figure 1f) indicated that the reduction in 5% H_2 did not change the light absorption at large in the UV light range, but the increase in the light absorption in the visible light region could be a result of the generation of mid-gap density of state, providing σ after moderate thermal activation.[36]

The bulk diffusion and surface exchange properties of the ZGO were further characterized by ECR method. The conductivity stabilization rate of ZGO under the reducing conditions slowed down as the temperature decreased (Figure 2a). The D_{chem} values (Figure 2b) of ZGO at 650 °C were similar to those of ceria at 800 °C[37] and $Gd_{0.1}Ce_{0.9}O_{2-\delta}$ at 900 °C,[38] while k_{chem} values were lower than them by 4-5 orders of magnitude. The surface exchange of oxygen would be the rate limiting process in the electrochemical process.

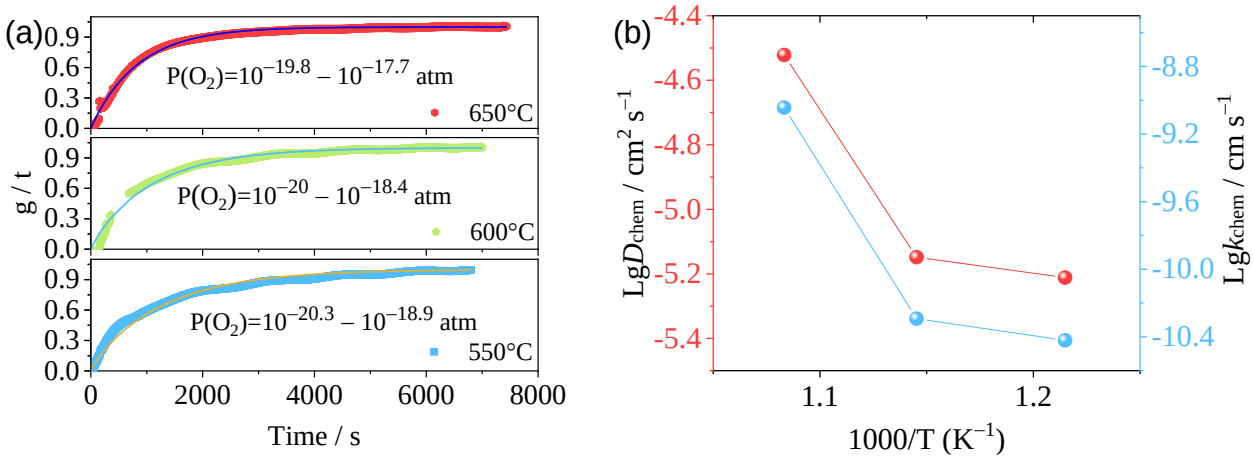

Figure 2. (a) ECR curves of ZGO at various temperature after a $P(O_2)$ step change. (b) Arrhenius plots

of the temperature dependence of the fitted D_{chem} and k_{chem}.

The microstructure of the ZGO powders reduced under the 5% H_2 atmosphere of 650 °C for 15h was used to study the superficial reduced layer (Figure 3a – 3h). The volatilization of Zn was insignificant, showing a Ga: Zn of 2.18 (atomic ratio) and no segregation of Zn or Ga was found in the EDS mapping. Small β-Ga_2O_3 crystallite was found on the surface of ZGO spinel, and more importantly, a continuous layer of (Zn, Ga)O_2 oxide with an ordered rock-salt (ORS) structure[39] was found due to the Zn^{2+} in the tetrahedral site moved towards the octahedral site to form the anti-site defects in the reduction process. In contrast, in the TEM images of ZGO reduced at 800 °C for 5 h (Figure 3i – 3l), β-Ga_2O_3 [40,41] dominated the surface due to the Zn evaporation. Zn deficiency was clearly observed in the selected regions (Figure 3j – 3l), showing an overall atomic ratio between Ga and Zn was 20 to 3 on the surface.

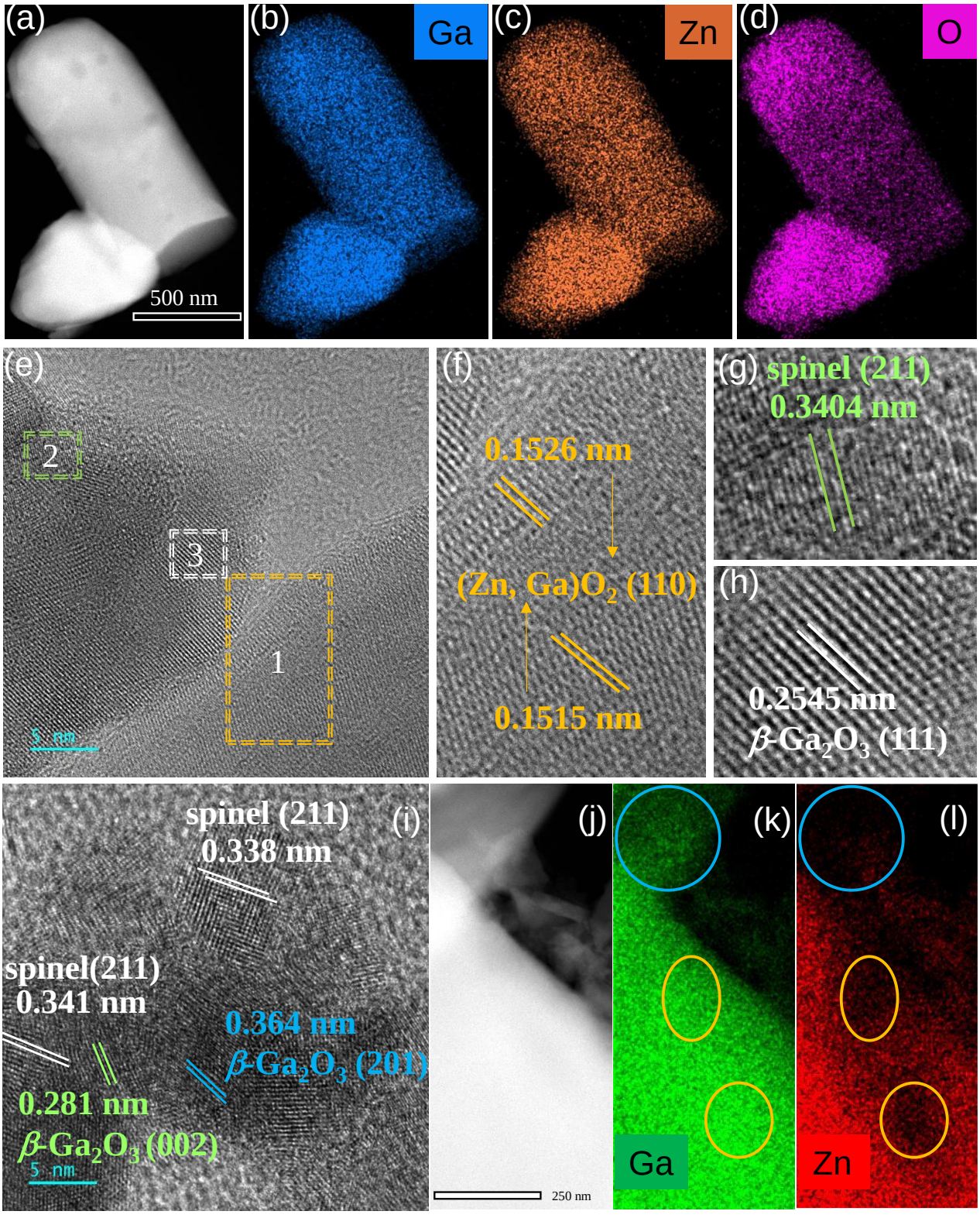

Figure 3. TEM images of the ZGO after reduction with 5% H_2 at 650 °C for 15 h (a – h) and 800 °C for 5 h (i – l). The 1st, 2nd, and 3rd rectangles correspond to the figure (f), (g), (h) in turn. The circles in (k) and (l) represented the areas on the sample surface where the Zn content varied significantly

compared to Ga.

XPS (Figure 4) was used to analyze the superficial properties of ZGO before and after the treatment in 5% H_2 at 800 °C. The core-level scan of O 1s showed two peaks at 530.5 eV and 532 eV, which could be assigned to the lattice oxygen[42] and the presence of weakly oxygen species or adsorbed chemically oxygen,[43,44] respectively. While the actual binding energy difference (ΔE) between the Zn $2p_{3/2}$ and Ga $2p_{3/2}$ peaks were all about 96 eV, which was in line with the spinel.[45] The reduction in 5% H_2 induced an decrease in the binding energy for the Zn 2p and Ga 2p orbitals (Figure 4b & 4c), because of the V_O as a donor.

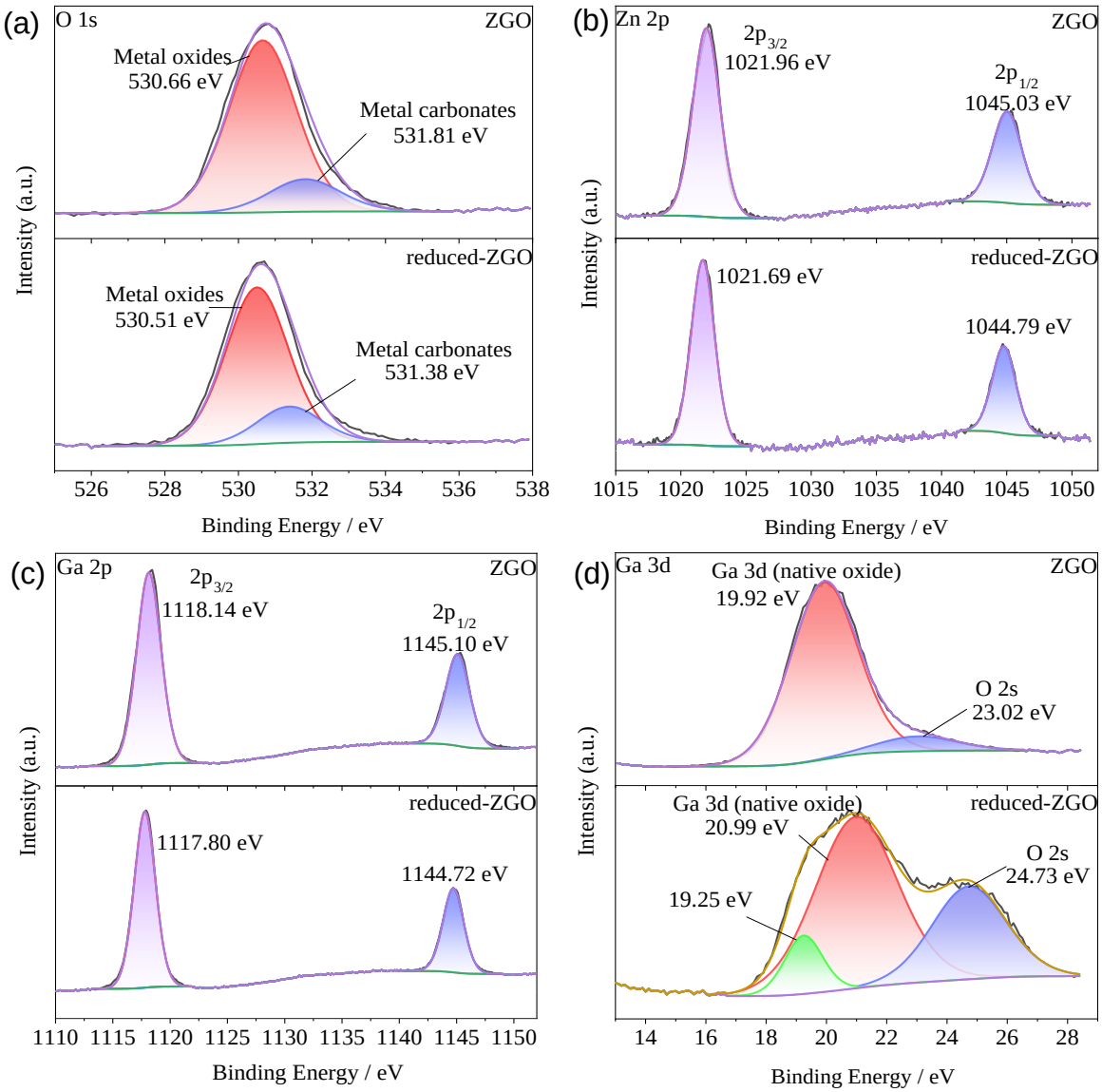

Figure 4. Core-level XPS scan of the as-prepared ZGO and the one after the reduction at 800 °C under 5% H_2 for 5h (reduced ZGO).

The Ga 3d orbital (Figure 4d) with a lower binding energy would probe deeper region underneath the surface.[46] According to the binding energy, Ga existed mainly in the form of ZGO oxide. The binding energy of Ga 3d in reduced ZGO was higher than the one in ZGO because of the migration of Ga in [GaO_6] octahedron to the tetrahedron site.[47] The additional peak at ~19.25 eV in reduced ZGO could be attributed to the hybridization of the Ga 3d and the O 2s states at the valence band (VB)[48,49]

or the presence of another Ga^{+}, Ga_2O[50] in the reduction process.

3.2 Fuel cell testing

The I−V−P curves (Figure 5a & 5b) indicated that a peak power of ZGO cell (2 mW cm^{-2}) at 600 °C could be enhanced by the 1% Ni impregnation (10 mW cm^{-2}). The limitation of the cells with and without 1% Ni impregnation could be attributed to the poor ionic conductivity as the ZGO/GDC cell showed a peak power of 12 mW cm^{-2} at 600 °C. Therefore, ZGO/GDC-1% Ni cell with GDC for the ionic conductivity and 1% Ni impregnation for the electrocatalysis towards the H_2 oxidation could provide a peak power of 302 mW cm^{-2} at 600 °C. The cell performance of the champion ZGO/GDC-1% Ni cell could reach 574 mW cm^{-2} at 650 °C, indicating that ZGO was sufficient to provide enough σ for the composite electrode. The juxtaposition of the EIS of the cells (Figure 5c – 5f) indicated that ZGO cell showed an ASR (around 130 Ω cm^{-2} at 600 °C) that was dominated by the polarization resistance (R_p). The ZGO/GDC-1% Ni cell showed the R_p of 0.24 Ω cm^2 at 650 °C and 0.52 Ω cm^2 at 600 °C, respectively. DRT profiles showed six polarization peaks with similar changes (P1-P6) at 600 or 650 °C, but the polarization peaks shifted slightly to low frequency due to the doping of GDC and the impregnation of 1% Ni. The P1 and P2 peaks in the low frequency region were important to the impedance of the system for the ZGO and ZGO/GDC cells, and the change of the two peaks may be related to gas diffusion in the fuel electrode.[51,52] The symmetric cell with porous GDC-LSFC as the electrode and SSZ as the electrolyte was prepared (Figure S2), and the EIS indicated the R_p of 0.15 Ω cm^2 and 0.48 Ω cm^2 at 650 °C and 600 °C, respectively. Therefore, the anode R_p of the ZGO/GDC-1% Ni anode was extremely small, and the full-cell impedance was mainly related to the oxygen reduction reaction at the cathode. The catalysis of Ni activated the adsorption of H_2, strengthening the

concentration gradient and increasing the diffusion of H_2.[53] Therefore, the intermediate frequency region (P3 and P4) dominated the cell impedance of the one with 1% Ni. The P3 and P4 peaks may be related to the gas adsorption/desorption[54] and the ion transport process of the anode.[52] The change of P5 and P6 peaks at the high frequency may be caused by the charge transfer process.[55]

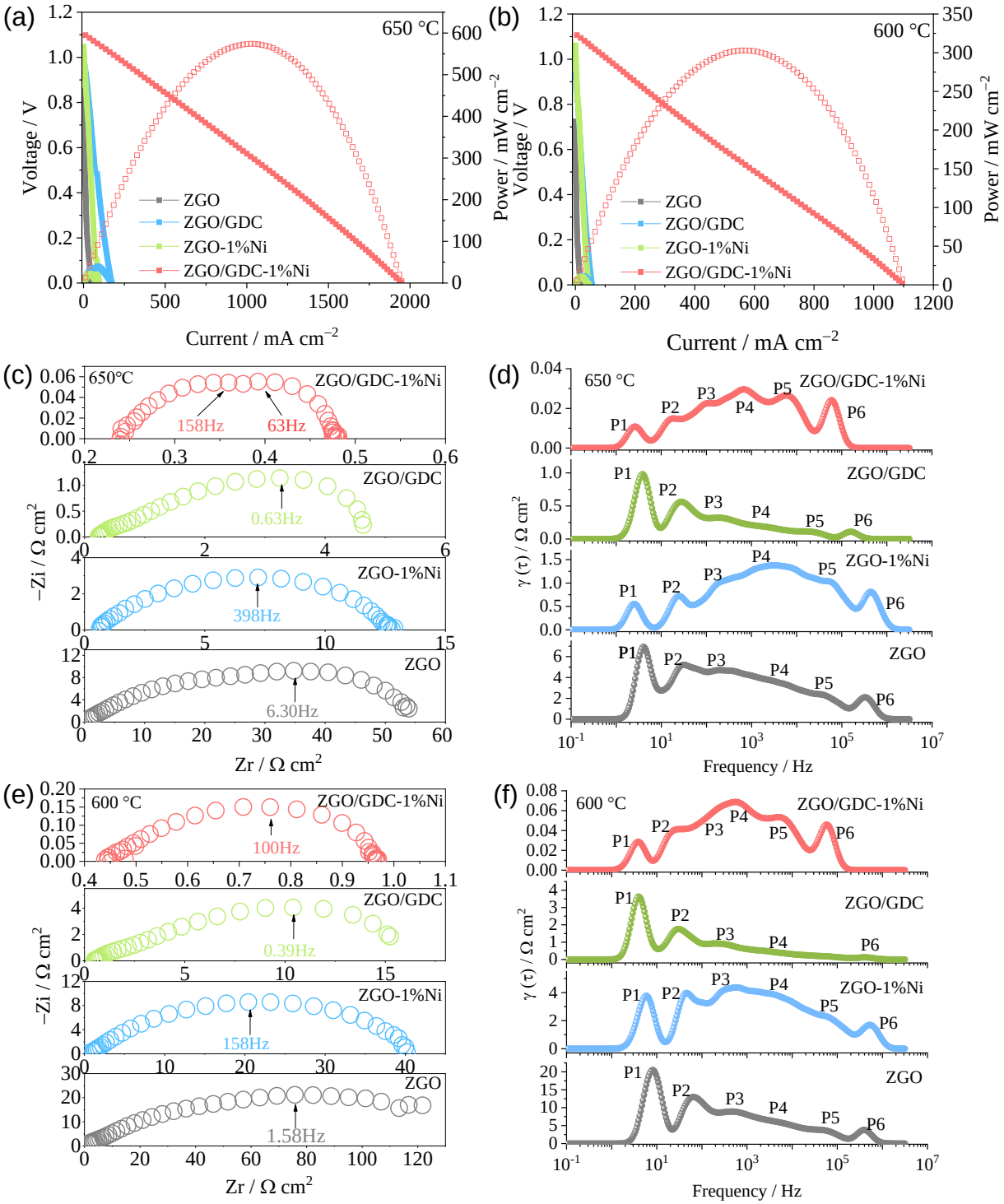

Figure 5. I−V−P curves of ZGO, ZGO/GDC, ZGO-1% Ni, ZGO/GDC-1% Ni cells at 650 °C (a) and 600 °C (b) using H_2 fuel. EIS of ZGO/GDC-1% Ni cells at 650 °C (c) and 600 °C (e) using H_2 as fuel and air as oxidant, respectively. DRT profiles of ZGO, ZGO/GDC, ZGO-1% Ni, ZGO/GDC-1% Ni cells at 650 °C (d) and 600 °C (f), respectively.

The ZGO/GDC-1% Ni cell degraded very quickly at 650 °C, but showed instability even at 600 °C (Figure 6): *i.e.* a drop of current density from 500 mA cm^{-2} to 300 mA cm^{-2} at –0.6 V was found within 300 hours of operation. However, the current density of the cell tended to be stable after 200 h, because the degradation in the first 200 h could be related to the surface change of the electrode as the microstructure change due to the Ni sintering, because it showed similar degradation to the one with ZGO-1% Ni. The ohmic resistance (R_s) increased only by 0.1 Ω cm^2 after 300h reduction (Figure S3) because of the re-oxidation of ZGO.

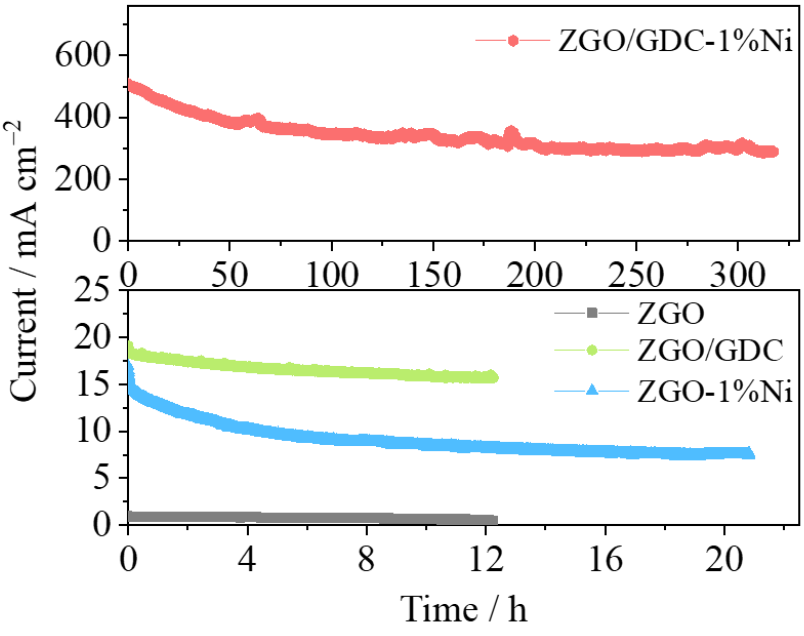

Figure 6. Chronoamperometry of ZGO, ZGO/GDC, ZGO-1%Ni, ZGO/GDC-1%Ni cells at 600 °C under –0.6V.

The ZGO-1% Ni cell using H_2 as fuel showed a significant optimization in R_p and current density

after 8 redox cycles at 600 °C (Figure S4). Slight increase in the performance after the redox cycles than the initial cycle was attributed to the change in the R_p.

The direct use of ethanol fuel depends on the its reforming to produced small molecules such as CO and H_2.[56] The ZGO/GDC-1% Ni cell could obtain a peak power of 100 mW cm^{-2} (Figure 7a) and an R_p of 4.3 Ω cm^2 (Figure 7b) at 600 °C under ethanol fuel, while the cell with ZGO along did not show any OCV (not presented). The H_2 generated by ethanol on ZGO/GDC-1% Ni powders (12%) was significantly more than that on ZGO powders (1.5%) at 600 °C (Figure S5). Compared with the H_2 fuel, the increase of R_p at OCV was related to lower H_2 concentration and difficulty in the direction oxidation of ethanol alone.[57] The propane fueling ZGO/GDC-1% Ni cell showed a peak power of 20 mW cm^{-2} and the R_p of 7.4 Ω cm^2.

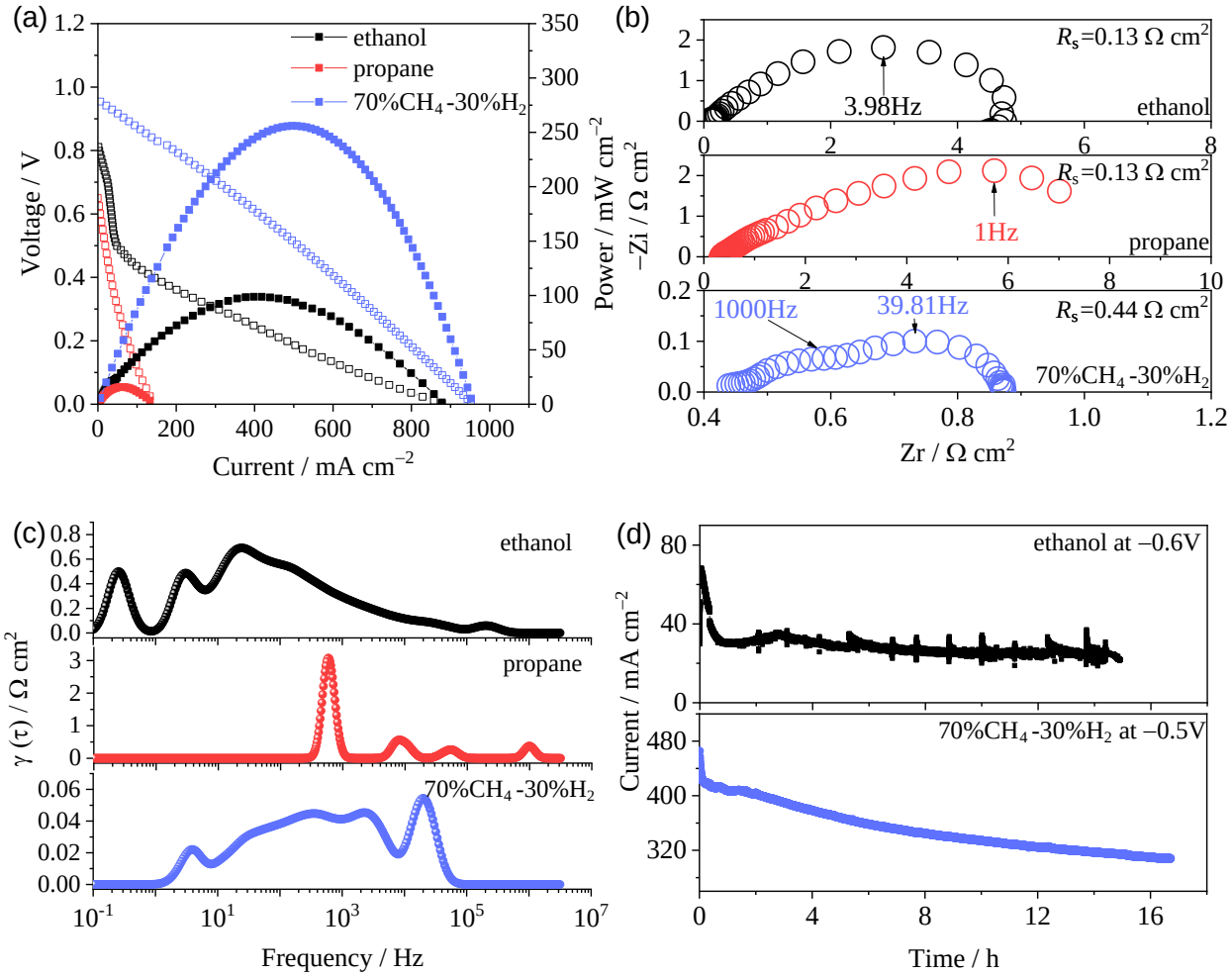

Figure 7. I−V−P curves (a), EIS (b) at OCV and DRT profiles (c) for the ZGO/GDC-1% Ni cell using ethanol, propane, and 70% CH_4-30% H_2 fuel at 600 °C, respectively. Chronoamperometry (d) of ZGO/GDC-1% Ni cell in the cases of ethanol and 70% CH_4-30% H_2 at 600 °C. The low OCV under the propane prohibited the chronoamperometry. The R_s was marked in (b).

The use of methane requires external or *in situ* (internal) anode reforming, resulting in H_2 and CO.[58] Setting in the undertaking of H_2 injection in natural gas pipelines, the introduction or oxidation of H_2 could provide steam for the *in situ* reforming of CH_4. Therefore, the cell under a 70% CH_4-30% H_2 fuel was measured to exhibit a low R_p of 0.44 Ω cm^2 and a high peak power of 260 mW cm^{-2}, which was slightly lower than the one under pure H_2. The R_s under 70% CH_4-30% H_2 was higher than that under ethanol and propane, which may be due to the more intense Zn evaporation under CH_4

condition.

DRT (Figure 7c) analysis indicated that the low-frequency impedance was predominant in the cell under ethanol, which may be related to the low diffusion coefficient of ethanol species. The polarization peaks under 70% CH_4-30% H_2 fuel was similar to that under H_2, mainly due to the impedance of the cathode.

The ZGO/GDC-1% Ni cell could maintain a current density of 30 mA cm^{-2} within 12 hours (Figure 7d) under ethanol fuel at −0.6 V. Though a high current density of about 380 mA cm^{-2} could be obtained at −0.25 V (Figure S6), the cell was damaged rapidly within twenty minutes, due to the rapid oxidation of the anode. Under the 70% CH_4-30% H_2, the cell showed a current dropping from 480 mA cm^{-2} to 300 mA cm^{-2} within 16-hours of operation at −0.5V. The stability of this cell was better than the one under H_2 as the CH_4 could scavenge the produced steam on the electrode surface to prevent its oxidation.

Post-mortem analysis

According to the SEM of the spent cell (Figure 8), the porous ZGO or ZGO/GDC-1% Ni electrode showed good bonding to the electrolyte (60 μm in thickness) and the size of ZGO grain was 1 μm in diameter. The ZGO/GDC-1% Ni electrode maintained a nanoparticle-decorated surface as a result of the 1% Ni infiltration and no obvious carbon filament was observed under the 12-h operation under ethanol.

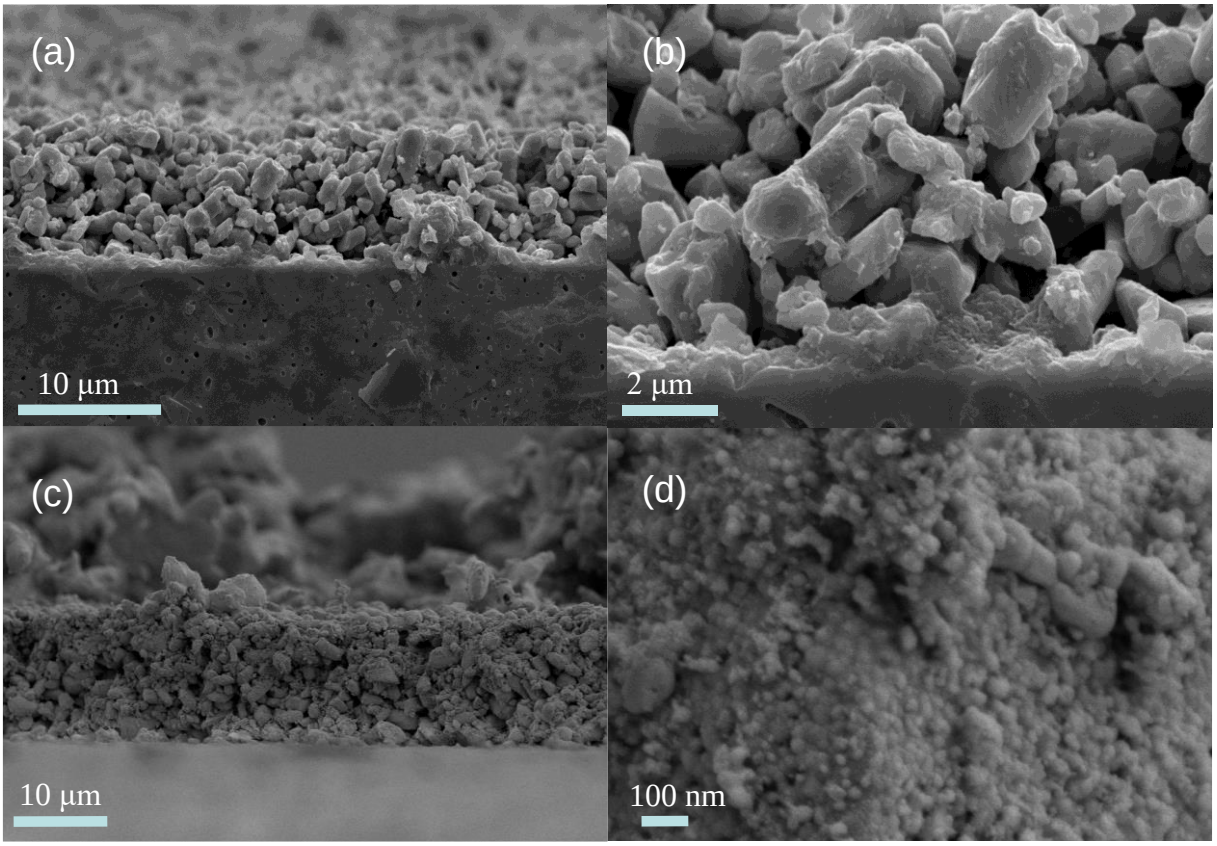

Figure 8. Cross-sectional SEM images of the anode after the durability: (a, b) ZGO cell with H_2 and (c, d) ZGO/GDC-1% Ni cell under ethanol fuel.

The XPS of ZGO/GDC-1% Ni anode after the durability test with ethanol and 70% CH_4-30% H_2 fuel showed an obvious difference of C 1s peak for the C-O-C bonds (Figure 9a). At the same time, in the O 1s peak (Figure 9b), the peak of the hydroxyl group (BE = 532.7 eV) of the cell using 70% CH_4-30% H_2 as fuel was enhanced significantly. Compared with ethanol fuel, the spin-orbit peaks in the Zn 2p and Ga 2p orbitals could be convoluted into two peaks (Figure 9c & 9d) after using 70% CH_4-30% H_2 as fuel[59] due to the formation of anti-site defects. The interaction between the Ga^{3+} located in the tetrahedron and the surrounding O^{2-} was weakened, which lead to the local aggregation of the oxygen ion electron cloud and increased the ionicity.[60] Furthermore, the superficial Ga/Zn atomic ratio was 12.89 and 8.14 after reaction with ethanol and 70% CH_4-30% H_2 fuel respectively, as a result of Zn loss from the surface.

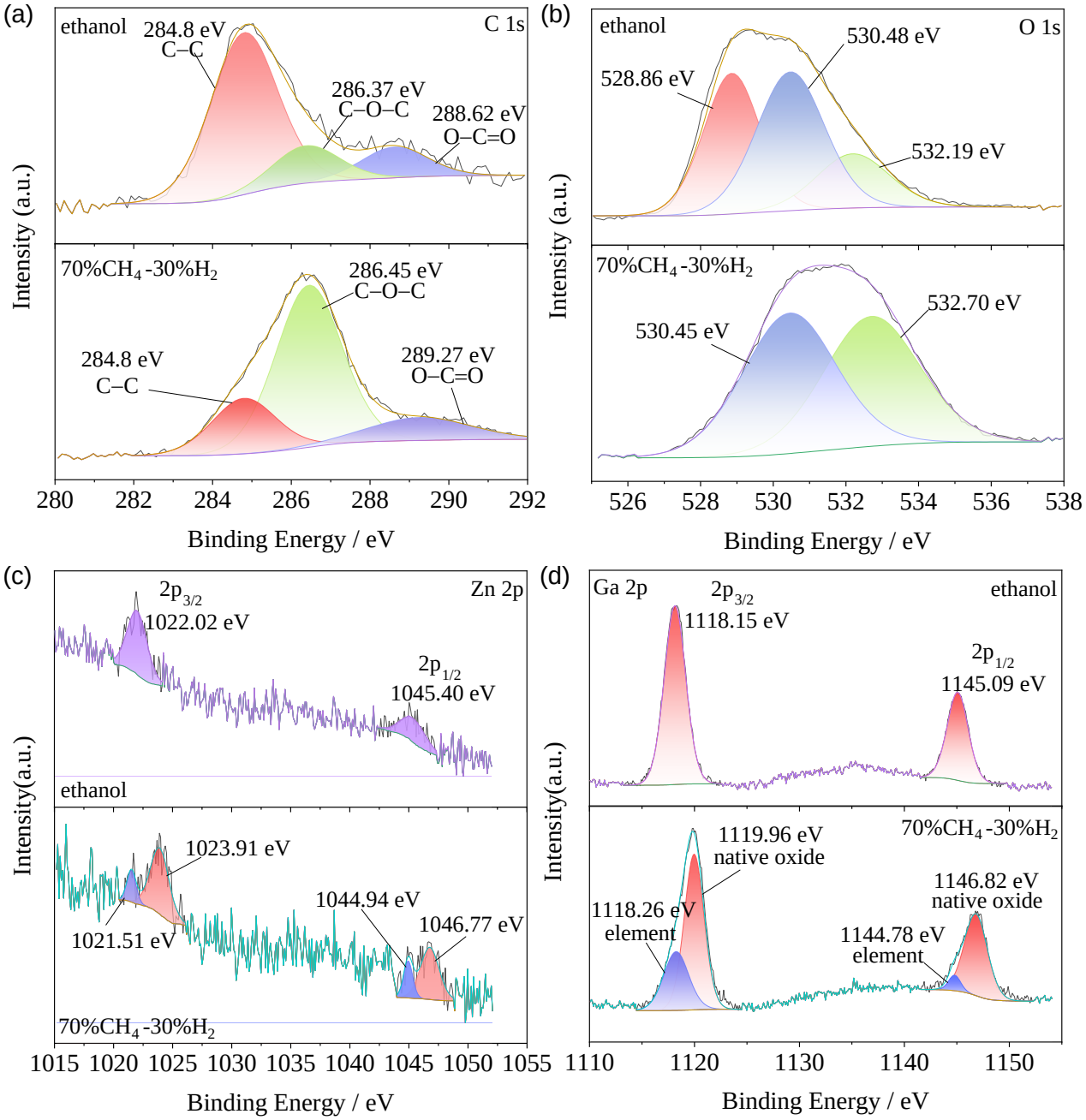

Figure 9. Core-level XPS scan of the ZGO/GDC-1% Ni anode after durability under ethanol and 70% CH_4-30% H_2 fuel at 600 °C.

4. Discussions

Comparing to those operating at high temperature (> 800 °C), LT-SOFCs (≤ 650 °C) can reduce

the system cost and degradation rate of the cell and increase the applicability of portable power.[19,61] The current exploration of *n*-type oxide anodes for the suppressing the coking focus mostly on titanate that needs a high reducing temperature, but the research on a reducible oxide for LT-SOFC is limited. Although the electrocatalysis of the oxide anode is anticipated to be low at a reduced temperature without the incorporation of metal co-catalyst, the redox stability and slight amount of the metals will impede the quick deterioration under carbonaceous fuel.

The Zn-O bond in ZGO was not strong enough to withstand the reduction in H_2 at a temperature above 650 ºC,[28] but was found to be stable at 600 °C. The ZGO single crystals could maintain the spinel structure at a Ga/Zn as high as 2.17, given the existence of "inverse" domain in the structure.[62,63] The higher Ga/Zn than 2.17 will cause the formation of β-Ga_2O_3. The Zn-deficient single crystals could attain a high σ of 10 to 500 S cm^{-1} as a result of the degenerate state for the mobility of free electrons (charge carrier density: ca. 10^{18}-10^{19} cm^{-3}).

The *in situ* reduction of ZGO under H_2 at a low temperature could be very difficult to cause the thorough change in the bulk material, and rather the change on the surface would make it be more conductive.[32] The reduction in H_2 will also cause the occupation of Ga^{3+} in the tetrahedral site for the formation of V_O on surface and providing σ.[59,60] The surface reduction could be confirmed by presence of β-Ga_2O_3 and (Zn, Ga)O_2 in the TEM image as a result of Zn loss from the surface and the anti-site between Zn and Ga. The (Zn, Ga)O_2 oxide generated a higher carrier concentration on the reduced surface. In this case, the conductivity in this study could be viewed as a core-shell structure with a very conductive surface whose inert core could be responsible for the redox stability of the anode. The reduced thin surface boasting V_O was insufficient to provide enough path for the swift O^{2-} transport [32] unless GDC as a super-ion conductor [64,65] was used as composite. The existence of free electron could

behave like metals to serve as electron sink to enhance the oxidation of fuel, the density of free electron was still much lower than Ni metal (free electron density: ca. 10^{22} cm^{-3}).

The R_p of anodes were listed in Table 1 along with those from the reported work. The R_p of ZGO anode was only one forth that of Nb-doped strontium titanate, while the one of ZGO/GDC anode was less than half of LSGM anode. As perovskite-type manganite and ferrite could be ionic conductor, they showed better electrocatalysis in the fuel oxidation than ZGO either with or without metal co-catalyst. The ZGO/GDC-1%Ni anode showed superior performance than most of the anode with metal catalyst at 650 and 600 °C, except for the one with Ni infiltrated LSGM. As an oxide anode, it could show much better stability than Ni-LSGM anode which showed fast increase in R_s due to the agglomeration in the redox cycle.[66]

Table 1. The R_p of oxide anodes in reducing atmosphere in the open literature.

	Anode material	**Electrolyte** [a]	**R_p (Ω cm^2) under H_2**		**Ref.**
			@ 650 °C	**@ 600 °C**	
Without metal	$PrBaMn_2O_{5+\delta}$	GDC|YSZ|GDC	/	4.98	[67]
	$Sr_{0.94}Ti_{0.9}Nb_{0.1}O_3$	ScYSZ	200	350	[68]
	LSGM	LSGM	10	/	[69]
	ZGO	SSZ	49.85	129.5	this work
	ZGO/GDC	SSZ	4.35	15.5	this work
With metal	Sr (Ti, Fe) O_3 with Ru	LDC|LSGM	1.3	/	[70]

Ni-CGO-$Sr_{0.94}Ti_{0.9}Nb_{0.1}O_3$	ScYSZ	0.5	0.97	[68]
2.51 vol% Ni- LSGM	LSGM	0.026	/	[69]
Ni-LSGM	LSGM	0.08	/	[71]
NiO-SDC-800 °C	YSZ	1	2.72	[72]
NiO/GDC	YSZ	0.83	1.14	[73]
14 wt% NiO-GDC	YSZ	/	0.31	[74]
Pd-Ni/GDC	YSZ	1.66	/	[75]
ZGO-1% Ni	SSZ	12.85	39.5	this work
ZGO/GDC-1% Ni	SSZ	0.1	0.04	this work

[a]: Those with buffer layers are in the configuration anode | electrolyte | cathode; LSGM, YSZ and ScYSZ represents $La_{0.8}Sr_{0.2}Ga_{0.8}Mg_{0.2}O_{3-\delta}$, 8 mol % Y_2O_3 - ZrO_2, and 10 mol % Sc_2O_3, 1 mol % Y_2O_3 stabilized ZrO_2, respectively.

The reforming of CH_4 is critically important for its utilization in fuel cell, and for a LT-SOFC can require a large amount of steam or even O_2 addition to produce enough H_2 or CO because the reforming kinetics will be lower at low temperature.[76] Alternatively, H_2 can be introduced to produce steam first and then the steam will be used for the *in situ* reforming of CH_4. Setting in the vast availability of H_2 from renewable sources and the H_2 injection in natural gas pipelines,[77] the H_2-CH_4 mixture can be an important way of mitigating the coking and increase the full utilization of methane fuel in nature gas. The development of *n*-type TCO type material anode that excels at reduced temperature under H_2-CH_4

mixture can be useful in this respect.

5. Conclusions

We demonstrated that an *n*-type ZGO insulator could be reduced at low temperature (≤ 650 °C), exhibiting high σ of 1.5 S cm^{-1} and 0.7 S cm^{-1} at 700 and 650 °C, respectively, though it was subjected to a superficial reduction for the production of a degenerated semiconductor with free electrons. Different from the conventional Ni-based anodes, ZGO-based anode exhibited high redox stability at 600 °C and could be used as an anode for the oxidation of an ethanol or propane fuel at a reduced temperature. The cells with ZGO-based anode showed some extent of deterioration in current density at an operation voltage of –0.6 V, which could be related to the re-oxidation of this *n*-type electrode or the sintering of Ni catalyst. The ZGO/GDC-1% Ni cell reached a peak power of 574 mW cm^{-2} under H_2 fuel at 650 °C and a peak power of 100 mWcm^{-2} under ethanol at 600 °C. The Zn evaporation could lead to the Ga-O rich surface for the passivation and retards the oxidation of the electrode under an anodic bias to show a stable performance after 200 hours. No significant carbon deposition was found for the ethanol-fueling cell for a short period of operation at 600 °C, showing that the application of TCO type material could be a new avenue in the anode design for LT-SOFC.

Conflicts of interest

There are no conflicts to declare.

Acknowledgements

This work is funded by National Natural Science Foundation of China (NSFC, 51702264), Funding for Central Universities (SWURC2020002) and Funding from Chongqing Scientific

Commission (cstc2021ycjh-bgzxm0162). C.N. and J.N. thanks the support from the merit of Bayu Scholar for Young Teachers and Yincai Talent from Chongqing municipal, respectively.

References

1. C. S. Ni, J. Zhou, Z. Y. Zhang, S. B. Li, J. P. Ni, K. Wu and J. T. S. Irvine, *Energy Environ. Sci.,* 2021, **14**, 6287-6319

2. A. Atkinson, S. Barnett, R. J. Gorte, J. T. S. Irvine, A. J. McEvoy, M. Mogensen, S. C. Singhal and J. Vohs, *Nat. Mater.,* 2004, **3**, 17-27.

3. V. Alzate-Restrepo and J. M. Hill, *J. Power Sources,* 2010, **195**, 1344-1351.

4. P. Boldrin, E. Ruiz-Trejo, J. Mermelstein, J. M. Bermudez Menendez, T. Rami Rez Reina and N. P. Brandon, *Chem. Rev.,* 2016, **116**, 13633-13684.

5. C.-A. Thieu, S. Yang, H.-I. Ji, H. Kim, K. J. Yoon, J.-H. Lee and J.-W. Son, *J. Mater. Chem. A,* 2022, **10**, 2460-2473.

6. M. Li, B. Hua, J.-L. Luo, S. P. Jiang, J. Pu, B. Chi and L. Jian, *J. Mater. Chem. A,* 2015, **3**, 21609-21617.

7. D. K. Niakolas, *Appl. Catal. A-Gen.,* 2014, **486**, 123-142.

8. A. Faes, A. Hessler-Wyser, A. Zryd and J. Van Herle, *Membranes-Basel,* 2012, **2**, 585-664.

9. M. Papac, V. Stevanovi, A. Zakutayev and R. O'Hayre, *Nat. Mater.,* 2021, **20**, 301-313.

10. A. A. Yaremchenko, S. G. Patricio and J. R. Frade, *J. Power Sources,* 2014, **245**, 557-569.

11. C. Ni, J. Feng, J. Cui, J. Zhou and J. Ni, *J. Electrochem. Soc.,* 2017, **164**, F283-F288.

12. G. Tsekouras and J. T. S. Irvine, *J. Mater. Chem.,* 2011, **21**, 9367-9376.

13. P. P. Edwards, A. Porch, M. O. Jones, D. V. Morgan and R. M. Perks, *Dalton T.,* 2004, 2995-3002.

14. P. Guo, R. D. Schaller, L. E. Ocola, B. T. Diroll, J. B. Ketterson and R. P. H. Chang, *Nat. Commun.,* 2016, **7**, 12892.

15. S. Yu, L. Li, X. Lyu and W. Zhang, *Sci. Rep.,* 2016, **6**, 20399.

16. M. Clerici, N. Kinsey, C. DeVault, J. Kim, E. G. Carnemolla, L. Caspani, A. Shaltout, D. Faccio, V. Shalaev, A. Boltasseva and M. Ferrera, *Nat. Commun.,* 2017, **8**, 15829.

17. T. Omata, N. Ueda, K. Ueda and H. Kawazoe, *Appl. Phys. Lett.,* 1994, **64**, 1077-1078.

18. A. Ndubuisi, S. Abouali, K. Singh and V. Thangadurai, *J. Mater. Chem. A,* 2022, **10**, 2196-2227.

19. E. D. Wachsman and K. T. Lee, *Science,* 2011, **334**, 935-359.

20. C. S. Ni, J. M. Vohs, R. J. Gorte and J. T. S. Irvine, *J. Mater. Chem. A,* 2014, **2**, 19150-19155.

21. D. Yoon and A. Manthiram, *J. Mater. Chem. A,* 2014, **2**, 17041-17046.

22. I. Yasuda and T. Hikita, *J. Electrochem. Soc.,* 1994, **141**, 1268-1273.

23. H. J. M. Bouwmeester, M. W. Den Otter and B. A. Boukamp, *J. Solid State Electrochem.,* 2004, **8**, 599-605.

24. M. Shah and S. A. Barnett, *Solid State Ionics,* 2008, **179**, 2059-2064.

25. A. KeZionis and E. Kazakevicius, *Electrochim. Acta,* 2020, **349**, 136379.

26. B. A. Boukamp, *J. Phys-Energy,* 2020, **2**, 042001.

27. Y. Zhao, K. Zhang, Z. Wei, Z. Li, Y. Wang, Z. Zhu and T. Liu, *Electrochim. Acta,* 2020, **352**, 136444.

28. T. Sei, Y. Nomura and T. Tsuchiya, *J. Non-Cryst. Solids,* 1997, **218**, 135-138.

29. Y. E. Lee, D. P. Norton, C. Park and C. M. Rouleau, *J. Appl. Phys.,* 2001, **89**, 1653-1656.

30. M. Yu, J. Lin, Y. H. Zhou and S. B. Wang, *Mater. Lett.,* 2002, **56**, 1007-1013.

31. M. Zhao, Y. Gu, P. Chen, Z. Xin, H. Zhu, B. Wang, K. Zhu, S. Yan and Z. Zou, *J. Mater. Chem. A,* 2019, **7**, 9316-9323.

32. Z. Yan, H. Takei and H. Kawazoe, *J. Am. Ceram. Soc.,* 1998, **81**, 180-186.

33. L. Lu, C. Ni, M. Cassidy and J. T. S. Irvine, *J. Mater. Chem. A,* 2016, **4**, 11708-11718.

34. S. W. Tao and J. T. S. Irvine, *Nat. Mater.,* 2003, **2**, 320-323.

35. H. L. Tuller and S. R. Bishop, *Annu. Rev. Mater. Res.,* 2011, **41**, 369-398.

36. B. R. Gao, J. Wang, M. M. Dou, X. Huang and X. X. Yu, *Sep. Purif. Technol.,* 2020, **241**, 116576.

37. S. Wang, M. Zheng, M. Li, X. Wu and C. Xia, *J. Mater. Chem. A,* 2016, **4**, 5745-5754.

38. Y. Wang, Y. Wang and C. Xia, *J. Electrochem. Soc.,* 2012, **159**, F570-F576.

39. C. Delmas, C. Fouassier and P. Hagenmuller, *Physica B & C,* 1980, **99**, 81-85.

40. J. H. Zhan, Y. Bando, J. Q. Hu, F. F. Xu and D. Golberg, *Small,* 2005, **1**, 883-888.

41. R. Roy, V. G. Hill and E. F. Osborn, *J. Am. Chem. Soc.,* 1952, **74**, 719-722.

42. X. Duan, F. Yu and Y. Wu, *Appl. Surf. Sci.,* 2012, **261**, 830-834.

43. C. Wu, T. W. Kim, T. Guo and F. Li, *Sci. Rep.,* 2016, **6**, 38613.

44. Z. Chi, F. G. Tarntair, M. Fregnaux, W. Y. Wu, C. Sartel, I. Madaci, P. Chapon, V. Sallet, Y. Dumont, A. Perez-Tomas, R. H. Horng and E. Chikoidze, *Mater. Today Phys.,* 2021, **20**, 100466.

45. L. Zou, X. Xiang, M. Wei, F. Li and D. G. Evans, *Inorg. Chem.,* 2008, **47**, 1361-1369.

46. H. R. S. Abdellatif, G. Zhang, Y. Tang, W. Ruan, J. Li, D. Xie, J. Ni and C. Ni, *Chem. Eng. J. (Lausanne),* 2020, **402**, 126199.

47. W. Yang, J. Li, B. Liu, X. Zhang, C. Zhang, P. Niu and X. Jiang, *Nanoscale,* 2018, **10**, 19039-19045.

48. A. Navarro-Quezada, S. Alame, N. Esser, J. Furthmuller, F. Bechstedt, Z. Galazka, D. Skuridina and P. Vogt, *Phys. Rev. B,* 2015, **92**, 195306.

49. A. Navarro-Quezada, Z. Galazka, S. Alame, D. Skuridina, P. Vogt and N. Esser, *Appl. Surf. Sci.,* 2015, **349**, 368-373.

50. N. Winkler, R. A. Wibowo, W. Kautek, G. Ligorio, E. J. W. List-Kratochvil and T. Dimopoulos, *J. Mater. Chem. C,* 2019, **7**, 69-77.

51. H. Sumi, T. Yamaguchi, K. Hamamoto, T. Suzuki, Y. Fujishiro, T. Matsui and K. Eguchi, *Electrochim. Acta,* 2012, **67**, 159-165.

52. M. Kornely, A. Neumann, N. H. Menzler, A. Leonide, A. Weber and E. Ivers-Tiffee, *J. Power Sources,* 2011, **196**, 7203-7208.

53. A. Kromp, S. Dierickx, A. Leonide, A. Weber and E. Ivers-Tiffee, *J. Electrochem. Soc.,* 2012, **159**, B597-B601.

54. X. X. Wang, Y. H. Ling, F. B. Zhou, P. Z. Feng and S. R. Wang, *J. Power Sources,* 2022, **537**, 231521.

55. C. B. Munoz, D. Pumiglia, S. J. McPhail, D. Montinaro, G. Comodi, G. Santori, M. Carlini and F. Polonara, *J. Power Sources,* 2015, **294**, 658-668.

56. B. X. Li, J. T. S. Irvine, J. P. Ni and C. S. Ni, *Appl. Energ.,* 2022, **306**, 118117.

57. T. Suzuki, T. Yamaguchi, K. Hamamoto, Y. Fujishiro, M. Awano and N. Sammes, *Energ. Environ. Sci.,* 2011, **4**, 940-943.

58. S. A. Saadabadi, N. van Linden, A. Heinsbroek and P. V. Aravind, *J. Clean. Prod.,* 2021, **291**, 125877.

59. N. N. Li, X. L. Duan, F. P. Yu and H. D. Jiang, *Vacuum,* 2017, **142**, 1-4.

60. J. S. Kim, H. I. Kang, W. N. Kim, J. I. Kim, J. C. Choi, H. L. Park, G. C. Kim, T. W. Kim, Y. H. Hwang, S. I. Mho, M. C. Jung and M. Han, *Appl. Phys. Lett.,* 2003, **82**, 2029-2031.

61. G. Yang, C. Su, H. Shi, Y. Zhu, Y. Song, W. Zhou and Z. Shao, *Energ. Fuel.,* 2020, **34**, 15169-15194.

62. Z. Galazka, S. Ganschow, R. Schewski, K. Irmscher, D. Klimm, A. Kwasniewski, M. Pietsch, A. Fiedler, I. Schulze-Jonack, M. Albrecht, T. Schroder and M. Bickermann, *Apl. Mater.,* 2019, **7**, 022512.

63. T. R. Paudel, A. Zakutayev, S. Lany, M. d'Avezac and A. Zunger, *Adv. Funct. Mater.,* 2011, **21**, 4493-4501.

64. B. C. H. Steele, *Solid State Ionics,* 1995, **75**, 157-165.

65. W. Lee, H. J. Jung, M. H. Lee, Y.-B. Kim, J. S. Park, R. Sinclair and F. B. Prinz, *Adv. Funct. Mater.,* 2012, **22**, 965-971.

66. C. Ni, Y. Zhang, X. Huang, J. Zou, G. Zhang and J. Ni, *Int. J. Hydrogen Energy,* 2017, **42**, 30760-30768.

67. Y. Gu, Y. Zhang, Y. Zheng, H. Chen, L. Ge and L. Guo, *Appl. Catal. B-Environ.,* 2019, **257**, 117868.

68. A. M. Hussain, J. V. T. Hogh, W. Zhang and N. Bonanos, *J. Power Sources,* 2012, **216**, 308-313.

69. Z. L. Zhan, D. M. Bierschenk, J. S. Cronin and S. A. Barnett, *Energ. Environ. Sci.,* 2011, **4**, 3951-3954.

70. R. Glaser, T. Zhu, H. Troiani, A. Caneiro, L. Mogni and S. Barnett, *J. Mater. Chem. A,* 2018, **6**, 5193-5201.

71. E. C. Miller, Q. Sherman, Z. Gao, P. W. Voorhees and S. A. Barnett, *ECS Trans.,* 2015, **68**, 1245.

72. M. Chen, B. H. Kim, Q. Xu and B. G. Ahn, *J. Membr. Sci.,* 2009, **334**, 138-147.

73. H. J. Park, *Electrochem. Solid St.,* 2011, **14**, B16-B19.

74. M. Lomberg, E. Ruiz-Trejo, G. Offer and N. P. Brandon, *J. Electrochem. Soc.,* 2014, **161**, F899-F905.

75. A. Babaei, S. P. Jiang and J. Li, *J. Electrochem. Soc.,* 2009, **156**, B1022-B1029.

76. C. C. Duan, R. J. Kee, H. Y. Zhu, C. Karakaya, Y. C. Chen, S. Ricote, A. Jarry, E. J. Crumlin, D. Hook, R. Braun, N. P. Sullivan and R. O'Hayre, *Nature,* 2018, **557**, 217-222.

77. Z. l. Messaoudani, F. Rigas, M. D. Binti Hamid and C. R. Che Hassan, *Int. J. Hydrogen Energy,* 2016, **41**, 17511-17525.